



Evidence of Extreme Ionization Conditions and Low Metallicity in GHZ2/GLASS-Z12 from a Combined Analysis of NIRSpec and MIRI

Downloaded from: <https://research.chalmers.se>, 2024-12-23 05:47 UTC

Citation for the original published paper (version of record):

Calabrò, A., Castellano, M., Zavala, J. et al (2024). Evidence of Extreme Ionization Conditions and Low Metallicity in GHZ2/GLASS-Z12 from a Combined Analysis of NIRSpec and MIRI Observations. *Astrophysical Journal*, 975(2).
<http://dx.doi.org/10.3847/1538-4357/ad7602>

N.B. When citing this work, cite the original published paper.



Evidence of Extreme Ionization Conditions and Low Metallicity in GHZ2/GLASS-Z12 from a Combined Analysis of NIRSpec and MIRI Observations

Antonello Calabrò¹, Marco Castellano¹, Jorge A. Zavala², Laura Pentericci¹, Pablo Arrabal Haro³, Tom J. L. C. Bakx⁴, Denis Burgarella⁵, Caitlin M. Casey⁶, Mark Dickinson⁷, Steven L. Finkelstein⁶, Adriano Fontana¹, Mario Llerena¹, Sara Mascia¹, Emiliano Merlin¹, Ikki Mitsuhashi^{2,8}, Lorenzo Napolitano^{1,9}, Diego Paris¹, Pablo G. Pérez-González¹⁰, Guido Roberts-Borsani¹¹, Paola Santini¹, Tommaso Treu¹¹, and Eros Vanzella¹²

¹ INAF—Osservatorio Astronomico di Roma, via di Frascati 33, 00078 Monte Porzio Catone, Italy; antonello.calabro@inaf.it

² National Astronomical Observatory of Japan, 2-21-1, Osawa, Mitaka, Tokyo, Japan

³ NSF's National Optical-Infrared Astronomy Research Laboratory, 950 N. Cherry Avenue, Tucson, AZ 85719, USA

⁴ Department of Space, Earth, & Environment, Chalmers University of Technology, Chalmersplatsen 4 412 96 Gothenburg, Sweden

⁵ Aix Marseille Univ, CNRS, CNES, LAM, Marseille, France

⁶ Department of Astronomy, The University of Texas at Austin, 2515 Speedway Boulevard Stop C1400, Austin, TX 78712, USA

⁷ NSF's NOIRLab, Tucson, AZ 85719, USA

⁸ Department of Astronomy, The University of Tokyo, 7-3-1 Hongo, Bunkyo, Tokyo 113-0033, Japan

⁹ Dipartimento di Fisica, Università di Roma Sapienza, Città Universitaria di Roma—Sapienza, Piazzale Aldo Moro, 2, 00185 Roma, Italy

¹⁰ Centro de Astrobiología (CAB), CSIC-INTA, Ctra. de Ajalvir km 4, Torrejón de Ardoz, E-28850, Madrid, Spain

¹¹ Department of Physics and Astronomy, University of California, Los Angeles, 430 Portola Plaza, Los Angeles, CA 90095, USA

¹² INAF—OAS, Osservatorio di Astrofisica e Scienza dello Spazio di Bologna, via Gobetti 93/3, I-40129 Bologna, Italy

Received 2024 March 19; revised 2024 August 27; accepted 2024 August 29; published 2024 November 6

Abstract

GHZ2/GLASS-z12, one of the most distant galaxies found in JWST observations, has been recently observed with both the NIRSpec and MIRI spectrographs, establishing a spectroscopic redshift $z_{\text{spec}} = 12.34$ and making it the first system at $z > 10$ with complete spectroscopic coverage from rest-frame UV to optical wavelengths. This galaxy is identified as a strong C IV $_{\lambda 1549}$ emitter (EW = 46 Å) with many other detected emission lines, such as N IV $_{\lambda 1488}$, He II $_{\lambda 1640}$, O III $_{\lambda\lambda 1661,1666}$, N III $_{\lambda 1750}$, C III $_{\lambda\lambda 1907,1909}$, [O II] $_{\lambda\lambda 3726,3729}$, [Ne III] $_{\lambda 3869}$, [O III] $_{\lambda\lambda 4959,5007}$, and H α , including a remarkable detection of the O III Bowen fluorescence line at rest frame $\lambda = 3133$ Å. We analyze in this paper the joint NIRSpec + MIRI spectral data set. Combining six optical strong-line diagnostics (namely R2, R3, R23, O32, Ne3O2, and Ne3O2Hd), we find extreme-ionization conditions, with $\log_{10}([\text{O III}]_{\lambda\lambda 4959,5007}/[\text{O II}]_{\lambda\lambda 3726,3729}) = 1.39 \pm 0.19$ and $\log_{10}([\text{Ne III}]_{\lambda 3869}/[\text{O II}]_{\lambda\lambda 3726,3729}) = 0.37 \pm 0.18$ in stark excess compared to typical values in the interstellar medium (ISM) at lower redshifts. These line properties are compatible either with an active galactic nucleus (AGN) or with a compact, very dense star-forming environment ($\Sigma_{\text{SFR}} \simeq 10^2\text{--}10^3 M_{\odot} \text{ yr}^{-1} \text{ kpc}^{-2}$ and $\Sigma_{M_*} \simeq 10^4\text{--}10^5 M_{\odot} \text{ pc}^{-2}$), with a high ionization parameter ($\log_{10}(U) = -1.75 \pm 0.16$), a high ionizing photon production efficiency $\log(\xi_{\text{ion}}) = 25.7^{+0.3}_{-0.1}$, and a low gas-phase metallicity (also confirmed by the direct, T_e method) ranging between 4% and 11% Z_{\odot} , indicating a rapid chemical enrichment of the ISM in the past few megayears. These properties also suggest that a substantial amount of ionizing photons ($\sim 10\%$) are leaking outside of GHZ2 and starting to reionize the surrounding intergalactic medium, possibly due to strong radiation-driven winds. The general lessons learned from GHZ2 are the following: (i) the UV-to-optical combined nebular indicators are broadly in agreement with UV-only or optical-only indicators; (ii) UV+optical diagnostics fail to discriminate between an AGN and star formation in a low-metallicity, high-density, and extreme-ionization environment; and (iii) comparing the nebular line ratios with local analogs may be approaching its limits at $z \gtrsim 10$, as this approach is potentially challenged by the unique conditions of star formation experienced by galaxies at these extreme redshifts.


Unified Astronomy Thesaurus concepts: Primordial galaxies (1293); Early universe (435); High-redshift galaxies (734); Lyman-break galaxies (979)

1. Introduction

The exciting discovery of galaxies in the early Universe was among the science drivers and the most eagerly expected results. The expectations have been surpassed by the earliest results from JWST, with multiple NIRCам imaging surveys (M. Castellano et al. 2022, 2023b; R. P. Naidu et al. 2022; S. L. Finkelstein et al. 2022; Y. Harikane et al. 2022;

C. M. Casey et al. 2024; C. T. Donnan et al. 2023b, 2023a; M. Franco et al. 2024) revealing dozens of galaxy candidates at redshifts beyond ~ 10 , when the Universe was less than ~ 500 Myr old. Their measured number density and luminosity are in stark excess compared to those expected from virtually any pre-JWST theoretical or empirical model (P. Arrabal Haro et al. 2023a, 2023b; R. J. Bouwens et al. 2023; S. L. Finkelstein et al. 2023).

This discovery calls for significant changes to our understanding of the physics of early galaxies. Multiple physical scenarios have been proposed to explain the excess of bright galaxies, including a higher stellar-to-halo mass ratio and star

 Original content from this work may be used under the terms of the [Creative Commons Attribution 4.0 licence](https://creativecommons.org/licenses/by/4.0/). Any further distribution of this work must maintain attribution to the author(s) and the title of the work, journal citation and DOI.

formation efficiency at early epochs (C. A. Mason et al. 2023; Y. Harikane et al. 2023, 2024), an increased weight of Population III and metal-poor stars with a top-heavy initial mass function (IMF; A. Trinca et al. 2023), negligible UV dust optical depth due to radiation-driven outflows at super-Eddington luminosities (A. Ferrara et al. 2023), and the contribution of early active galactic nucleus (AGN) activity, primordial black holes, or other exotic particles to the UV photon budget (N. Cappelluti et al. 2022). To make progress in this field and also assess the role of the population of high- z galaxies in cosmic reionization, we must move from simple detection to physical characterization by probing their rest-frame UV and optical emission lines with spectroscopic observations.

The lack of Balmer and metal lines at $\lambda > 4000 \text{ \AA}$, which all fall beyond the spectral coverage of NIRSpec (the most sensitive spectrograph on board the JWST), have hampered so far a thorough characterization of the most distant sources. For this reason, a first simple strategy to approach the primordial Universe has been that of probing the average conditions of galaxies at increasing redshifts and then trying to extrapolate those at $z > 10$. Indeed, NIRSpec has already opened a new frontier by probing with unprecedented depth the ionization and metallicity of statistical samples of galaxies down to low mass ($\sim 10^7 M_\odot$) from $z \simeq 4$ to $z \simeq 10$. Several studies (e.g., J. R. Trump et al. 2023; K. Nakajima et al. 2023; M. Curti et al. 2023, 2023b) have found that typical galaxies at the epoch of reionization (EoR) have relatively low Z_{gas} values, but not significantly different from those observed at $z \gtrsim 2$, remaining close to or above 10% Z_\odot . If these trends persist beyond $z \simeq 10$, it will be difficult to explain the excess of UV luminosity density in the pre-EoR as due to extremely metal-poor stellar populations. On the other hand, several studies have found a significant evolution in ionizing strength from cosmic noon to $z \sim 9$ (A. J. Pahl et al. 2020; A. J. Cameron et al. 2023; J. R. Trump et al. 2023; N. A. Reddy et al. 2023). This leaves us with the questions of how cosmic ionization evolves at earlier times and what are the properties of galaxies that may have started the reionization in the first 500 Myr of our Universe. The next unavoidable step is to directly observe spectroscopically this unexpectedly UV-bright population at $z > 10$. A handful of galaxies have been recently observed (with NIRSpec) in the redshift range from 10 to 12, such as Maisie’s Galaxy and CEERS2_588 (P. Arrabal Haro et al. 2023b), GN-z11 (A. J. Bunker et al. 2023), and MACS0647-JD (T. Y.-Y. Hsiao & D. Coe et al. 2023). However, longer-wavelength observations with the Mid-Infrared Instrument (MIRI) are required to obtain a complete rest-frame optical spectral coverage.

The combination of NIRSpec and MIRI spectroscopy was recently achieved for GHZ2/GLASS-z12 (hereafter simply GHZ2), which is another remarkable example and one of the most representative of the UV-bright galaxy population at $z > 10$. Lying in a small area of $\simeq 10 \text{ arcmin}^2$ in the background of the galaxy cluster A2744, it was initially identified in imaging by M. Castellano et al. (2022) and R. P. Naidu et al. (2022) within the GLASS-JWST Early Release Science program (T. Treu et al. 2022). Independent teams have estimated its photometric redshift z_{phot} in a range between 11.9 and 12.4, using different methods (M. Castellano et al. 2022; R. P. Naidu et al. 2022; Y. Harikane et al. 2022; C. T. Donnan et al. 2023a; H. Atek et al. 2023). According to

the spectral energy distribution (SED) fitting estimates, GHZ2 has among the highest UV luminosity at such high redshift ($M_{\text{UV}} = -20.5 \text{ mag}$), and it may have already built $\geq 10^9 M_\odot$ in stars, a factor of ~ 3 higher than expected from the maximum stellar-to-halo mass ratio (SHMR) at this redshift (P. Behroozi et al. 2020).

This galaxy was observed with the JWST Near Infrared Spectrograph (NIRSpec) in low-resolution prism configuration on 2023 October 24 by the Program GO-3073 (PI M. Castellano), which has revealed the detection of multiple emission lines at $z = 12.34$, including $\text{N IV}]_{\lambda 1488}$, $\text{He II}_{\lambda 1640}$, $\text{O III}]_{\lambda\lambda 1661,1666}$, $\text{N III}]_{\lambda 1750}$, $\text{C III}]_{\lambda\lambda 1907,1909}$, $\text{O III}]_{\lambda 3133}$, $[\text{O II}]_{\lambda\lambda 3726,3729}$, $[\text{Ne III}]_{\lambda 3869}$, and a bright $\text{C IV}]_{\lambda 1549}$ with an equivalent width (EW) = 46 Å, placing this source in the category of strong C IV emitters (M. Castellano et al. 2024). Despite the multiple lines detected, the UV spectral properties of GHZ2 are inconclusive on the star-forming or AGN nature of the source. Even the surprising detection of the O III Bowen fluorescence line at 3133 Å is not decisive evidence of an AGN, as its emission could be also associated with X-ray binaries and planetary nebulae (X.-W. Liu & J. Danziger 1993; C. B. Pereira et al. 1999; P. Selvelli et al. 2007). In addition, the absence of the high-ionization $\text{N V}]_{\lambda 1240}$ and $[\text{Ne V}]_{\lambda 3426}$ lines and the low upper limit on the $[\text{Ne IV}]_{\lambda 2424}/\text{N IV}]_{\lambda 1488}$ ratio are likely inconsistent with the AGN hypothesis and more in line with a star-forming scenario, according to the models of A. Feltre et al. (2016) and Julia Gutkin et al. (2016).¹³ To probe the rest-frame optical lines, GHZ2 was also targeted with the JWST MIRI Low Resolution Spectrometer (LRS) and observed in the same period (2023 October 25–29) by the program GO-3703 (PI J. Zavala). As described in J. A. Zavala et al. (2024), we detect $\text{H}\alpha$ and $[\text{O III}]_{\lambda\lambda 4959,5007}$. No broad $\text{H}\alpha$ components were detected, limited by the low spectral resolution, leaving still open the interpretation on the nature of this object.

These observations make GHZ2 the most distant galaxy for which we have spectroscopic measurements covering the full UV-to-optical spectral range. The purpose of this paper is to combine the information from the emission lines detected in NIRSpec and MIRI, to provide a comprehensive understanding and a more robust assessment of its ionization and metallicity properties. In particular, we will analyze in a systematic way the following six most widely adopted strong-line diagnostics (see L. J. Kewley & S. L. Ellison 2008, for a thorough discussion): $\text{R2} = \log([\text{O II}]_{\lambda\lambda 3726,3729}/\text{H}\beta)$, $\text{R3} = \log([\text{O III}]_{\lambda 5007}/\text{H}\beta)$, $\text{R23} = \log(([\text{O III}]_{\lambda\lambda 4959,5007} + [\text{O II}]_{\lambda\lambda 3726,3729})/\text{H}\beta)$, $\text{O32} = \log([\text{O III}]_{\lambda\lambda 4959,5007}/[\text{O II}]_{\lambda\lambda 3726,3729})$, $\text{Ne3O2} = \log([\text{Ne III}]_{\lambda 3869}/[\text{O II}]_{\lambda\lambda 3726,3729})$, and $\text{Ne3O2Hd} = \log(([\text{Ne III}]_{\lambda 3869} + [\text{O II}]_{\lambda\lambda 3726,3729})/\text{H}\delta)$. With this line data set, we will analyze the metallicity and ionization with calibrations based on local analogs of high-redshift systems, and we will further investigate the star-forming or AGN nature of the source. Additionally, this will enable us to conduct comparisons with data inferred solely from NIRSpec or MIRI, or from fitting NIRCам photometry with stellar population models. Such analyses will offer insights into the optimal strategies for future spectroscopic follow-ups of the earliest galaxies. The spectrophotometric analysis combining NIRCам + NIRSpec + MIRI will be presented in a different paper.

The paper is organized as follows: In Section 2, we briefly summarize the NIRSpec and MIRI observations of GHZ2, the derivation of the emission-line fluxes, and the physical

¹³ We note that those models assume subsolar-to-solar N/O abundance ratios that might differ from those in GHZ2 and other nitrogen-enriched galaxies.

properties obtained independently in the two studies. In Section 3, we combine the emission lines detected in the two spectra to better assess the ionization and metallicity of GHZ2 via line ratios, and we discuss the possibility of distinguishing between AGN and stellar photoionization. We present our conclusions in Section 4.

Throughout the paper we adopt AB magnitudes (J. B. Oke & J. E. Gunn 1983), a G. Chabrier (2003) IMF, a solar metallicity of $12 + \log(\text{O}/\text{H}) = 8.69$ (M. Asplund et al. 2009), and a flat Λ CDM concordance model ($H_0 = 70.0 \text{ km s}^{-1} \text{ Mpc}^{-1}$, $\Omega_M = 0.30$).

2. Methodology

2.1. Observations and Data Reduction

While the full description of the observations and spectral reduction is presented in M. Castellano et al. (2024, hereafter C24) and J. A. Zavala et al. (2024, hereafter Z24), we highlight here the most important features. GHZ2 was observed with NIRSpec in PRISM-CLEAR configuration (i.e., with spectral resolution R ranging from 30 at $\lambda = 0.6 \mu\text{m}$ to 330 at $\lambda = 5.3 \mu\text{m}$), adopting three-shutter “slits” with a three-point nodding for optimal background subtraction, reaching a total exposure time of 19,701 s in three separate visits. The data were reduced with the standard calibration pipeline provided by STScI (ver. 1.13.4; H. Bushouse et al. 2024) following the methodology of P. Arrabal Haro et al. (2023a), which provides the full wavelength- and flux-calibrated 2D and 1D spectrum. The output NIRSpec spectrum was also corrected for residual slit and aperture losses by matching the detected continuum level with the latest available broadband NIRCам photometry (E. Merlin et al. 2024), as already done in L. Napolitano et al. (2024).

The MIRI observations were conducted with the LRS slit mode, which provides a resolving power of $R \simeq 50\text{--}200$ over $5\text{--}12 \mu\text{m}$, with an “along-slit” dithering mode and a total integration time on source of 9 hr. The spectral reduction was performed using the same version of the STScI pipeline adopted for NIRSpec, with background subtraction applied on each dither position and final extraction of the 2D and 1D spectrum performed as described in Z24.

2.2. Main Physical Properties of GHZ2

Multiple emission lines were detected through the NIRSpec and MIRI observations, as explained in Section 1, which have allowed us to constrain the spectroscopic redshift z_{spec} of the galaxy. We adopt here the $z_{\text{spec}} = 12.342 \pm 0.009$ derived from a weighted average of the measurements of the best-resolved, high signal-to-noise ratio (S/N) lines in the NIRSpec spectrum (C24), and in good agreement with the MIRI-derived estimate of 12.33 ± 0.02 (Z24). This is also in agreement with the value estimated from the high-resolution spectrum obtained with the Very Large Telescope X-SHOOTER instrument by the program 110.244H.001 (PI E. Vanzella), in which CIV $_{\lambda 1548}$ was detected at an S/N = 4.4. We remark that for investigating the nebular properties in the combined NIRSpec + MIRI spectrum we consider throughout this work the line fluxes and uncertainties reported in the two companion papers.

We adopt a stellar mass M_* of $\log_{10} M_*/M_{\odot} = 8.91_{-0.28}^{+0.13}$, derived by Z24 through fitting the NIRCам photometry and the emission lines with the SYNTHESIZER-AGN code (P. G. Pérez-González et al. 2003), with G. Bruzual & S. Charlot (2003)

stellar populations models, assuming a Chabrier IMF with stellar mass limits between 0.1 and $100 M_{\odot}$, a double burst with delayed-exponential law, and nebular emission grids computed with CLOUDY v23 (M. Chatzikos et al. 2023). This stellar mass is consistent with the estimate of $\log M_*/M_{\odot} = 9.05_{-0.25}^{+0.10}$ derived, independently, by C24 with BAGPIPES (A. C. Carnall et al. 2018) using only the photometric data, assuming the Binary Population and Spectral Synthesis (BPASS) stellar population models v2.2.1 (J. J. Eldridge et al. 2017; E. R. Stanway & J. J. Eldridge 2018) and a double power-law star formation history (SFH). We also adopt the best-fit mass-weighted age of 28_{-14}^{+10} Myr from the first study, which implies that $\simeq 60\%$ of the total M_* was formed in the past 30 Myr (Z24).

We adopt for GHZ2 the star formation rate (SFR) obtained by Z24 from the H α line in the MIRI spectrum, which yields $\text{SFR} = 9 \pm 3 M_{\odot} \text{ yr}^{-1}$. This assumes the calibration of N. A. Reddy et al. (2022) as $\text{SFR} = L_{\text{H}\alpha} \times 10^{-41.67}$, which is the most suited for the subsolar metallicities expected in the early Universe, reflecting the greater efficiency of ionizing photon production in metal-poor stellar populations and harder ionizing spectra due to binary star interactions. From the SED fitting presented above, Z24 derive an SFR that is consistent with the H α -based value and a very low dust attenuation in V band ($A_V = 0.1_{-0.1}^{+0.2}$), which adds to the very blue UV slope measured for the galaxy ($\beta = -2.39 \pm 0.07$) by C24. Assuming negligible dust attenuation and case B recombination, Z24 rescale the H α flux to estimate intrinsic H β and H δ fluxes, which are consistent with the observed upper limits of the two undetected lines.

Several studies have found that low-mass, extreme emission-line galaxies at high redshift may have Balmer decrements significantly smaller than case B recombination by factors of up to $\sim 10\%$ (M. Stiavelli et al. 2023; H. Yanagisawa et al. 2024; M. W. Topping et al. 2024). While the physical origin of these Balmer decrement anomalies is still unclear and possibly due, among other things, to density-bounded geometries or optically thick, excited neutral gas clouds (see C. Scarlata et al. 2024; H. Yanagisawa et al. 2024; W. McClymont et al. 2024), we note that assuming the most conservative H α /H β observed ratio of 2.55 (H. Yanagisawa et al. 2024; M. W. Topping et al. 2024) would produce small variations ($\sim 6\%$) of Balmer based line indices and $\sim 10\%$ lower gas-phase metallicities. Therefore, this would not significantly affect our results and would not alter the main conclusions of this paper. We remark that additional SED fitting methods were tested in Z24, which yield lower stellar masses (by ~ 0.6 dex) and dust attenuations A_V in the range of 0–0.3 mag. Following these results, we incorporate an uncertainty of $+0.3$ mag on A_V in the following analysis. Alternative and more sophisticated fitting procedures will be investigated in future works.

We assume an effective radius of $r_e = 105 \pm 9$ pc measured by L. Yang et al. (2022), from which we calculate the SFR surface density Σ_{SFR} as $\text{SFR}/(2 \times \pi \times r_e^2)$, yielding $\log \Sigma_{\text{SFR}}/(M_{\odot} \text{ yr}^{-1} \text{ kpc}^{-2}) = 2.11_{-0.25}^{+0.35}$. We note that a smaller radius ($= 34 \pm 9$ pc) was measured by Y. Ono et al. (2023),¹⁴ in

¹⁴ We note that r_e refers to the semimajor axis in L. Yang et al. (2022), while it is defined as the circularized radius in Y. Ono et al. (2023). For a sanity check, we have independently fitted a Sérsic profile to GHZ2 with the code galight (X. Ding et al. 2021), finding that this galaxy is unresolved, with an upper limit on r_e (corrected for lensing) of 80 pc, thus more consistent with Y. Ono et al. (2023). To be conservative, we consider both previous measurements in our analysis. In any case, our final conclusions are not affected by the choice of r_e .

which case $\log \Sigma_{\text{SFR}}/(M_{\odot} \text{ yr}^{-1} \text{ kpc}^{-2})$ would rise to 3.1 ± 0.4 . We finally remark that all the physical properties introduced above have been properly corrected to account for gravitational lensing, using the moderate magnification ($\mu = 1.3$) estimated by P. Bergamini et al. (2023).

2.3. Comparison to Photoionization Models

To understand the nebular and ionizing source properties of GHZ2, it is useful to compare our observed emission-line ratios with those predicted by photoionization models. To this aim, we consider the line predictions derived with the photoionization models described in A. Calabrò et al. (2023), which are computed with the Python package `pyCLOUDY` v.0.9.11,¹⁵ running with version 17.01 of the CLOUDY code (G. J. Ferland et al. 2017).

In brief, star-forming galaxies are modeled with a spherically symmetric, radiation-bounded shell of gas surrounding a population of young (O- and B-type) stars, with the incident radiation field derived from BPASS stellar population models (J. J. Eldridge et al. 2017) and with an IMF extending to $100 M_{\odot}$ and continuous star formation in the past 30 Myr, to match the measured average age of GHZ2 (Z24). We also analyze the emission predicted by AGN models, in which the continuum is built using the default “AGN” prescription in CLOUDY, with a multiple power-law continuum assuming a “blue bump” temperature of 10^6 K and spectral energy indices of $\alpha_{\text{UV}} = -0.5$, $\alpha_{\text{x}} = -1.35$, and $\alpha_{\text{ox}} = -1.4$ (B. A. Groves et al. 2004) in UV, in X-rays, and from the optical to the X-ray range, respectively. We consider the metallicity range from 0.05 and 1 times solar (i.e., 0.05, 0.1, 0.15, 0.2, 0.3, 0.4, 0.5, 0.7, 1) for star-forming (SF) galaxies and from 0.05 and 2 times solar (i.e., 0.05, 0.1, 0.2, 0.3, 0.4, 0.5, 0.7, 1, 2) for AGNs, with the solar reference consistent with our definition in Section 1. In all cases, we derive predictions for four different ionization parameters $\log(U) = -3, -2.5, -2, \text{ and } -1.5$ and for three gas density values ($10^2, 10^3, \text{ and } 10^4 \text{ cm}^{-3}$). Regarding dust depletion, the metals are depleted in the beginning of our CLOUDY calculations, and we consider that this depletion is metallicity dependent, as discussed in A. Calabrò et al. (2023). In particular, for the elements analyzed in this work, Ne is a refractory element in all conditions (Julia Gutkin et al. 2016), while the depletion factor of oxygen (0.2 dex at solar metallicity) is expected to decrease significantly when going to subsolar metallicity, especially at $\lesssim 0.1 Z_{\odot}$ (G. Vladilo et al. 2011; A. De Cia et al. 2016); hence, we assume that it is negligible for GHZ2. This is also reasonable considering the very low dust attenuation (and hence dust content) that we infer for this galaxy.

We also explore the density-bounded scenario for the nebula. We have modeled this case by varying the stopping criterion in CLOUDY from a Lyman continuum (LyC) optical depth = 10 (fully ionization bounded case) to 0.1 (fully density-bounded case). This would correspond to an escape fraction of ionizing photons going from 0% to 100%, according to A. Plat et al. (2019). As noted by the other studies (e.g., E. W. Pellegrini et al. 2012; A. E. Jaskot & M. S. Oey 2013; K. Nakajima et al. 2020), a density-bounded scenario tends to increase the flux of high-ionization species with respect to low-ionization species. In our case, it would increase the O32 and Ne3O2 indices, mimicking the effect of a high ionization parameter. However, we find that, with the modest escape fraction ($\sim 10\%$) estimated for GHZ2 (see Section 4), the increase in O32 and Ne3O2

would be lower than 0.1 dex and thus would not change the main interpretation of this paper. We finally note that, following a similar argument to that in N. A. Reddy et al. (2023), the high electron density ($\geq 10^3 \text{ cm}^{-3}$; Z24) and the high SFR of this galaxy suggest that we are closer to a radiation-bounded geometry.

We refer to A. Calabrò et al. (2023) for a more detailed description of the models, including element abundances and dust depletion. Considering different AGN models among those tested in A. Calabrò et al. (2023), or different setups for the star-forming models, does not significantly affect the predicted line ratios and does not alter the conclusions of this paper.

3. Results and Discussion

3.1. Combining NIRSpec and MIRI Emission-line Ratios

We explore in this first subsection the ionizing and excitation conditions of the interstellar medium (ISM), while in the following one we investigate whether the ionization field is of stellar or AGN origin. The measured values of the various line ratio indices used in this paper are reported in Table 1.

3.1.1. Excitation versus Ionization Diagnostics

One of the most valuable nebular diagnostics is built by comparing the R23 and O32 line indices, which probe the excitation and ionization states of the gas, respectively. This diagram has been widely used to study the ISM conditions both in the local Universe and at higher redshifts (e.g., R. Maiolino et al. 2008; M. Onodera et al. 2016; R. L. Sanders et al. 2016; K. Nakajima et al. 2020; D. Schaerer et al. 2022b; S. R. Flury et al. 2022b; N. A. Reddy et al. 2023). To put in context our results, we consider the NIRSpec sample recently observed by the CEERS and GLASS-JWST spectroscopic surveys (S. Mascia et al. 2023; A. Calabrò et al. 2024), representative of the star-forming galaxy population at the EoR in the mass range $7 < \log(M_{*}/M_{\odot}) < 10.5$, and a sample of similarly low mass star-forming galaxies (M_{*} down to $10^7 M_{\odot}$) at intermediate redshifts ($z \sim 0.7$) from the VIMOS Ultra Deep Survey (VUDS; A. Calabrò et al. 2017). Finally, we explore the parameter space occupied by galaxies from the Sloan Digital Sky Survey (SDSS) as a benchmark for typical star-forming systems in the local Universe (G. Kauffmann et al. 2003). We also consider a subset of metal-poor and high-ionization systems selected in the local Universe to mimic the properties of high-redshift galaxies (F. Bian et al. 2018).

We show the R23–O32 diagram in the top panel of Figure 1. We can notice an overall increase of the ISM ionization when we go from the local Universe, probed by the SDSS, to intermediate redshifts ($z \sim 0.7$), probed by the VUDS, and then to galaxies at $z \geq 4$, probed by the NIRSpec galaxies. GHZ2 lies in the upper part of the diagram, with an O32 index of 1.39 ± 0.19 and an R23 index of 0.88 ± 0.12 . While the latter value is similar to what is found also in lower-redshift systems, the O32 is higher than in typical star-forming galaxies at the EoR, as well as compared to the median properties of the so-called local analogs of high-redshift galaxies (F. Bian et al. 2018), highlighted in Figure 1 with open black stars for bins of decreasing metallicity. GHZ2 also has a similar O32 to that measured for the strongly lensed galaxy MACS1149-JD1 (at $z = 9.1$) identified by M. Stiavelli et al. (2023).

Comparing the position of GHZ2 in this diagram to photoionization model predictions for star-forming galaxies,

¹⁵ <https://github.com/Morisset/pyCloudy/tree/0.9.11>

Table 1
Line Indices Measured for GHZ2

Index	Line Ratio	Z (A) (Z_{\odot})	Z (B) (Z_{\odot})	Z (C) (Z_{\odot})	Z (D) (Z_{\odot})
R2	-0.52 ± 0.20	$0.06_{0.03}^{0.11}$	$0.06_{0.04}^{0.09}$
R3 ^a	0.72 ± 0.11	...	$0.12_{0.09}$	$0.08_{0.05}^{0.16}$	$0.05_{0.03}^{0.12}$
R23	0.88 ± 0.12	...	$0.11_{0.06}$	$0.08_{0.05}^{0.19}$	$0.05_{0.03}^{0.13}$
O32	1.39 ± 0.19	$0.11_{0.07}^{0.14}$	$0.07_{0.05}^{0.10}$
Ne3O2 ^b	0.37 ± 0.18	$0.07_{0.06}^{0.10}$	$0.04_{0.02}^{0.05}$
Ne3O2Hd	0.59 ± 0.12
average		0.08 ± 0.02	0.11 ± 0.04	0.07 ± 0.03	0.054 ± 0.009

Notes. Table with gas-phase metallicities (in units of Z_{\odot}) estimated for GHZ2 using multiple indices (first row) and the following calibrations: (A) F. Bian et al. (2018); (B) M. Curti et al. (2020); (C) K. Nakajima et al. (2022); (D) R. L. Sanders et al. (2024). The average value from all the indices available for the same calibration set is shown in the last row. A metallicity of $0.06_{-0.02}^{+0.04}$ is obtained with the T_e method from the $\text{O III}]_{\lambda 1666}/[\text{O III}]_{\lambda 5007}$ line ratio. The R3, R23, O32, Ne3O2, and Ne3O2Hd indices are used to study the excitation and ionization properties in Section 3.1.1 and 3.1.2.

^a See also J. A. Zavala et al. (2024).

^b See also M. Castellano et al. (2024).

we find that it lies in the low-metallicity branch ($Z < 0.3 Z_{\odot}$), where R23 turns over and starts to decline in more metal-poor systems, and its ISM is consistent with a high ionization parameter ($\log(U) \sim -2$) and a high electron density n_e of the gas between 10^3 and 10^4 cm^{-3} , or, at a fixed n_e of 10^3 cm^{-3} , with an even higher ionization in the range of $-2 \leq \log(U) \leq -1.5$. We note that a similar range of n_e ($\geq 10^3 \text{ cm}^{-3}$) is suggested by Atacama Large Millimeter/submillimeter Array (ALMA) observations (G. Popping 2023; J. A. Zavala et al. 2024) by the nondetection of the $[\text{O III}]_{\lambda 88 \mu\text{m}}$ line (assuming an electron temperature $T_e = 10^4 \text{ K}$). The inferred range of $\log(U)$ would be in agreement with the estimates of -1.78 ± 0.28 and $-1.4_{-0.3}^{+0.2}$ based on two SED fitting approaches by C24 and Z24.

We calculate directly the ionization parameter from the O32 index using an extrapolation toward higher O32 of the empirical relation derived by C. Papovich et al. (2022) with galaxies at redshifts $1.1 < z < 2.3$ observed by the CLEAR survey. This yields $\log_{10}(U) = -1.75 \pm 0.16$, which is within the range suggested by the previous model comparison and by the SED fitting method. This again points toward very strong ionizing conditions that are typically not seen in low-redshift galaxies.

We now compare the results of the R23–O32 diagram with those from another “excitation versus ionization” diagram, involving the $\log([\text{Ne III}]_{\lambda 3869} + [\text{O II}]_{\lambda \lambda 3726, 3729})/\text{H}\delta$ (Ne3O2Hd) index and Ne3O2. This diagram can be used for galaxies at $9 \lesssim z \lesssim 12$, in which the $\text{H}\beta$ and $[\text{O III}] \lambda 5007 \text{ \AA}$ lines fall outside of the NIRSspec coverage (see recent applications in A. J. Bunker et al. 2023 for GN-z11 and in G. Roberts-Borsani et al. 2024). $\text{H}\delta$ is typically fainter than $[\text{Ne III}]$ or $[\text{O II}]$, but its flux can be rescaled from that of Balmer lines at longer wavelengths after accounting for dust attenuation.

For GHZ2, we follow the example of Z24 and derive $\text{H}\delta$ from $\text{H}\alpha$ assuming case B recombination (D. E. Osterbrock & G. J. Ferland 2006) and negligible dust attenuation, which is supported by the blue UV continuum slope (C24) and the ALMA detection limits (T. J. L. C. Bakx et al. 2023). This yields a Ne3O2Hd index of 0.59 ± 0.12 . We also measure for this galaxy a Ne3O2 value of 0.37 ± 0.18 . A similar procedure was used to derive Ne3O2Hd in lower-redshift comparison samples.

The position of GHZ2 in the Ne3O2Hd–Ne3O2 parameter space is shown in the bottom panel of Figure 1. GHZ2 is in the

upper left envelope of the distribution that extends from the local SDSS and the intermediate- z VUDDS galaxies in the lower right corner of the diagram to the upper left part occupied by the NIRSspec galaxies at $z > 4$, following a sequence of increasing Ne3O3 (and decreasing Ne3O2Hd) as a function of redshift. We highlight that GHZ2 has even more extreme properties than typical star-forming galaxies at the EoR. Its position is instead similar to that of GN-z11 (A. J. Bunker et al. 2023) and MACS1149-JD1 (M. Stiavelli et al. 2023), in which they detect $\text{H}\delta$, even though GHZ2 has a more extreme ionization traced by Ne3O2. The EW and line ratios of GHZ2 are also similar to those of the compact galaxy RXCJ2248-ID at $z = 6.1$ (M. W. Topping et al. 2024), as noted by C24. In the analyzed diagrams, this would be the only object more extreme than GHZ2, having an $\text{O32} \simeq 2.3$ and $\text{Ne3O2} \simeq 1.2$. The Ne3O2 index measured for GHZ2 also exceeds the parameter range covered by the sample of F. Bian et al. (2018), indicating that local analogs of high-redshift galaxies do not have the same extreme conditions found in this galaxy. Similarly to the R23–O32 diagram, also the Ne3O2Hd–Ne3O2 one favors high electron densities $\geq 10^3 \text{ cm}^{-3}$, low metallicity ($0.05 < Z/Z_{\odot} < 0.1$), and high ionization parameter $\log(U) \sim -2$.

Overall, this diagram provides a picture that is consistent with that obtained with the classic R23 versus O32 diagram, indicating the presence of a hard ionizing radiation field in GHZ2 and more extreme ionization properties than typically found in star-forming galaxies.

3.1.2. Investigating the Star-forming or AGN Nature with the OHNO Diagram

The O32 and Ne3O2 index values are a clear sign of a hard ionizing source powering GHZ2 (see also C24 and Z24). Understanding whether this hard ionization field is due to star formation or an AGN is fundamental to reach a physical interpretation on the nature of massive and blue galaxies in the bright end of the luminosity function at $z > 10$. We have shown in the two companion papers that it is not possible to distinguish between AGN and massive young stellar population photoionization on the basis of the NIRSspec-PRISM and MIRI-LRS spectrum alone, lacking enough sensitivity and spectral resolution.

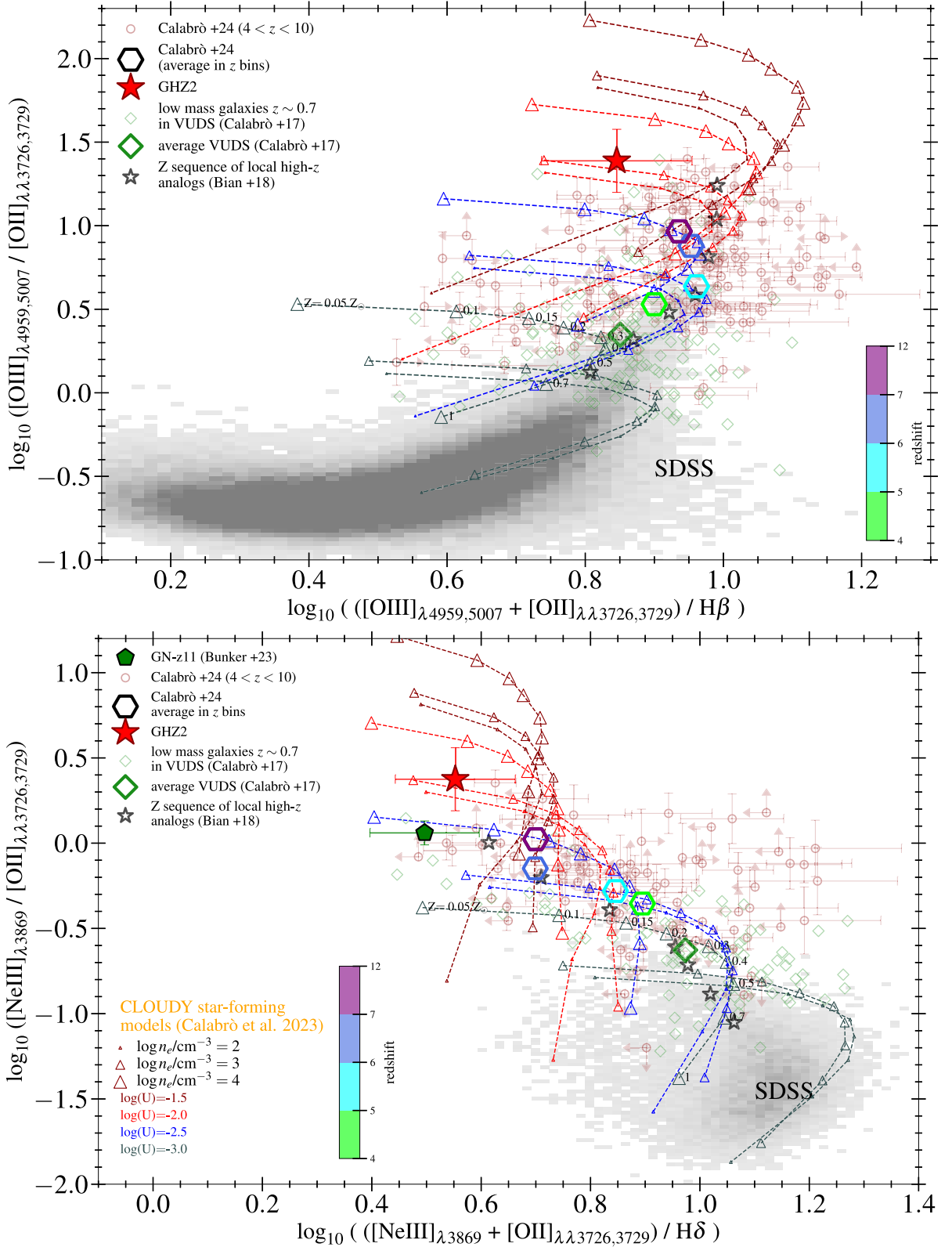


Figure 1. Top: the R23 vs. O32 diagram. Bottom: the Ne3O2Hd vs. Ne3O2 diagram. GHZ2 (big red star) is compared to the NIRSpc sample of SF galaxies from A. Calabrò et al. (2024). Local SDSS SF galaxies are shown with a binned 2D gray histogram, while $z \sim 0.7$ low-mass star-forming galaxies from A. Calabrò et al. (2017) are shown with green open diamonds. Overplotted are SF model predictions computed with pyCLOUDY from A. Calabrò et al. (2023), assuming ranges of $\log(U)$ ($-3, -2.5, -2, -1.5$), Z ($0.05, 0.1, 0.15, 0.2, 0.3, 0.4, 0.5, 0.7, 1 Z_{\odot}$), and $\log n_e/\text{cm}^{-3}$ ($2, 3, 4$), as shown in the legend in the bottom panel. Both diagrams suggest a $\log(U) \simeq -2$ and a low metallicity between 0.05 and $0.1 Z_{\odot}$.

The combination of NIRSpc and MIRI allows us to test the nature of GHZ2 with another diagram by comparing the R3 and Ne3O2 line indices, dubbed the OHNO diagram. This

diagnostic has been successfully applied to classify galaxies from the local Universe to cosmic noon (G. R. Zeimann et al. 2015; B. E. Backhaus et al. 2022; N. J. Cleri et al. 2023).

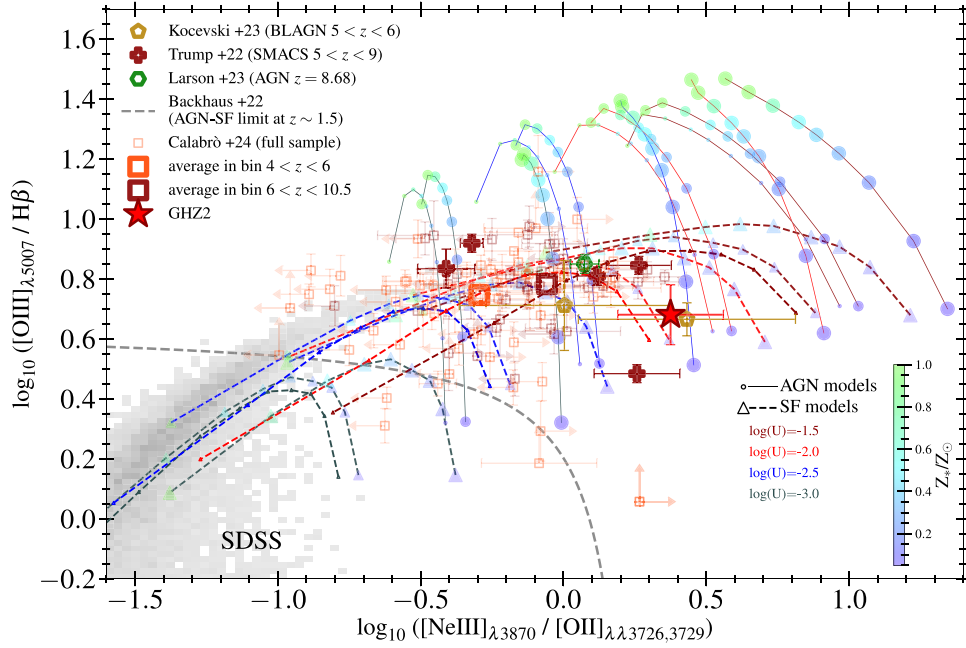


Figure 2. The $\log [O\ III]_{\lambda 5007}/H\beta$ (R3)– $\log [Ne\ III]_{\lambda 3870}/[O\ II]_{\lambda\lambda 3726,3729}$ (Ne3O2) diagram (“OHNO”). The position of GHZ2 is shown with a big red star, while other observations of star-forming galaxies and broad-line AGNs identified at $z > 5$ by recent JWST observations are included as big colored polygons. The predictions of photoionization models from A. Calabrò et al. (2023) are overplotted for comparison. The models are shown for three representative electron densities $n_e = 10^2, 10^3,$ and 10^4 cm^{-3} (increasing size symbols) and cover a variety of metallicities (from 0.05 to solar, following the color bar in the lower right corner) and ionization parameters ($-3, -2.5, -2, -1.5$, following the convention of Figure 1).

At redshift ~ 1.5 , a separation criterion was also proposed by B. E. Backhaus et al. (2022), according to which AGNs have significantly higher R3 and Ne3O2 than star-forming galaxies. These studies have found that from $z = 1$ to $z = 10$ Ne3O2 increases on average while R3 remains relatively constant. This can be attributed to higher gas densities and ionization parameters in H II regions at higher redshifts, as well as perhaps to a greater contribution of AGNs to photoionization.

For GHZ2 we measure an R3 index of 0.72 ± 0.11 . The resulting position in the OHNO diagram is shown in Figure 2, compared to photoionization model predictions. Other high-redshift sources recently observed by JWST in the epoch of reionization are also included (D. D. Kocevski et al. 2023; J. R. Trump et al. 2023; R. L. Larson et al. 2023; A. Calabrò et al. 2024). First, we can see that the source lies in the AGN region according to the separation criteria derived at $z \sim 1.5$ by B. E. Backhaus et al. (2022) and is consistent with the prediction of AGN models with subsolar metallicities ($0.05 < Z_{\text{gas}}/Z_{\odot} < 0.1$), high ionization parameters ($\log_{10} U \sim -2$), and electron densities n_e of 10^2 – 10^3 cm^{-3} . Another possible interpretation would be a higher $n_e \sim 10^4\text{ cm}^{-3}$ and a slightly lower $\log_{10} U \sim -2.5$. Its position closely resembles that of confirmed broad-line AGNs at $z > 5$ from D. D. Kocevski et al. (2023) and R. L. Larson et al. (2023). However, the galaxy is also consistent with star-forming models, overlapping with the parameter space expected for H II regions with high electron density ($n_e \geq 10^3\text{ cm}^{-3}$), high ionization parameter ($\log_{10} U \sim -2$), and low metallicity ($0.05 < Z_{\text{gas}}/Z_{\odot} < 0.1$), in remarkable agreement with the results inferred from the two star-forming diagnostics analyzed above (Figure 1). GHZ2 also lies in the region occupied by the five star-forming galaxies at $z > 5$ (with no evidence of an AGN at $R \sim 1000$) studied by J. R. Trump et al. (2023) in the SMACS 0723 Early Release Observations (K. M. Pontoppidan et al. 2022), confirming that typical star-

forming galaxies in the EoR have nebular properties and ISM conditions resembling those of AGNs at $5 < z < 7$, as also indicated by our modeling.

Overall, these results indicate that even combining NIRSpect and MIRI, that is, considering the full rest-frame UV and optical wavelength coverage, we are not able to pin down the nature of the ionizing source in GHZ2. However, regardless of its physical nature, our modeling suggests in both cases the presence in GHZ2 of very low metallicity gas ($Z_{\text{gas}} \sim 0.05$ – $0.1 Z_{\odot}$), with high electron density and high ionization parameter.

3.2. Ionization Properties and SFR Surface Density

The evolution of $\log_{10}(U)$ across cosmic time can be explained as an effect of the increase of gas density and SFR surface density (e.g., N. A. Reddy et al. 2023), meaning that denser and more compact molecular clouds, and hence elevated Σ_{SFR} in high-redshift galaxies, might be directly responsible for the increase of the ionization parameter, playing a more important role than metallicity. Significant correlations were indeed found between n_e , Σ_{SFR} , and O32 (R. Shimakawa et al. 2015; T. Jiang et al. 2019; N. A. Reddy et al. 2023; A. Calabrò et al. 2024), confirming the close relation between these quantities. According to hydrodynamical simulations (e.g., X. Ma et al. 2016; M. Sharma et al. 2017), enhanced Σ_{SFR} and O32 also favor strong stellar feedback and outflows, which can carve channels in the ISM of the galaxies for the leakage of LyC radiation. Previous observations have reported a relation between Σ_{SFR} and the escape fraction f_{esc} of ionizing photons (T. M. Heckman 2001; R. P. Naidu et al. 2020; S. R. Flury et al. 2022a), showing that galaxies with higher Σ_{SFR} have larger fractions of LyC leakers and higher f_{esc} . Similarly, Y. I. Izotov et al. (2020) empirically found a close relation between O32 and the measured f_{esc} at low redshift. S. R. Flury

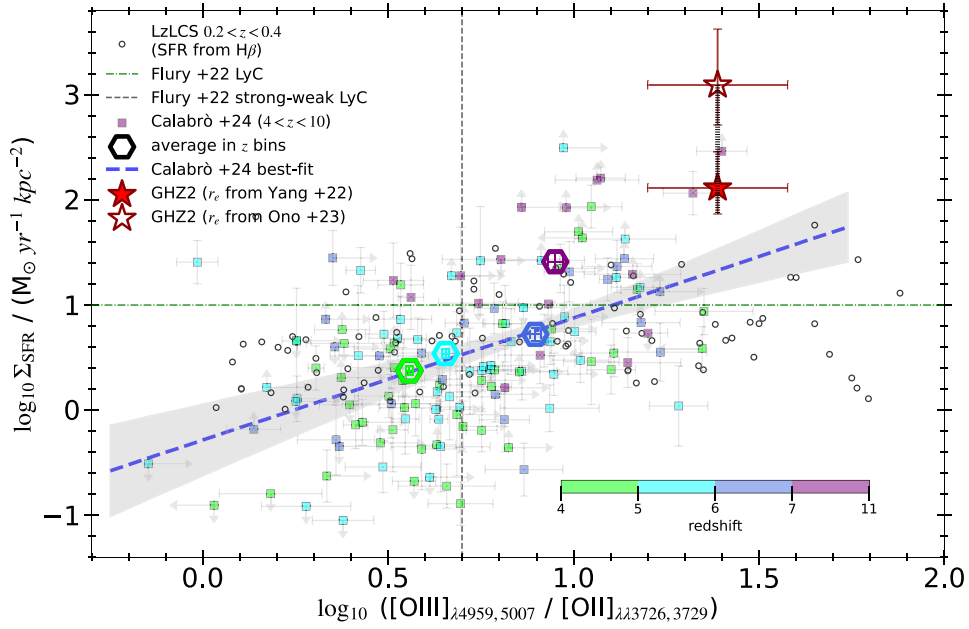


Figure 3. The Σ_{SFR} vs. O32 diagram. The position of GHZ2 is highlighted with a big red star. The sample of NIRSpec galaxies at redshifts $4 < z < 10$ from A. Calabrò et al. (2024) is added with color-coding based on redshift. The vertical and horizontal dashed lines represent the thresholds of Σ_{SFR} and O32, respectively, for being a strong LyC leaker candidate, as obtained from the analysis of 66 LyC leakers at $0.2 < z < 0.4$ (open black circles) by S. R. Flury et al. (2022b). According to these criteria, GHZ2 would be a strong LyC-leaking candidate.

et al. (2022a) put the two quantities together, establishing that galaxies with $\Sigma_{\text{SFR}} > 10 M_{\odot} \text{ yr}^{-1} \text{ kpc}^{-2}$ and $\text{O32} > 0.7$ are strong LyC leaker candidates, based on direct measurements of f_{esc} in a very large sample of local LyC-leaking galaxies from the Low Redshift Lyman Continuum survey (LZLCS). We can investigate the properties of GHZ2 in the O32 versus Σ_{SFR} diagram and infer some information on the escape fraction.

In Figure 3, we compare GHZ2 to NIRSpec galaxies at $4 < z < 10$ and to the LyC-leaking galaxies at $0.2 < z < 0.4$ observed by S. R. Flury et al. (2022b). We can see that GHZ2 lies in the upper right corner of the diagram, with Σ_{SFR} and O32 significantly higher compared to typical values found in lower-redshift galaxies. In detail, GHZ2 lies at the highest values of O32 and Σ_{SFR} found for NIRSpec galaxies from A. Calabrò et al. (2024) and above the Σ_{SFR} –O32 best-fit relation derived in that work. Considering the smaller size reported in the literature by Y. Ono et al. (2023) would make this galaxy even more extreme, surpassing in Σ_{SFR} and O32 all the sources observed at the EoR by the previous study.

The position of GHZ2 in Figure 3 implies that the galaxy is quite likely to leak LyC emission, satisfying all the conditions defined by S. R. Flury et al. (2022a). Using the f_{esc} relation by S. Mascia et al. (2023), calibrated on LyC-leaking galaxies from the LZLCS, we derive an indirect estimate of $f_{\text{esc}} = 0.10^{+0.02}_{-0.01}$. Alternatively, using the β -slope-based relation by J. Chisholm et al. (2022) yields a very consistent value of $0.11^{+0.02}_{-0.02}$. This average f_{esc} of 0.10 inferred for GHZ2 is consistent with that predicted for its Σ_{SFR} value, using the Σ_{SFR} – f_{esc} best-fit relation at $4 < z < 10$ by A. Calabrò et al. (2024). Moreover, in the NIRSpec spectrum there is a 2σ flux excess at the position of $\text{Mg II}_{\lambda 2800}$, which needs confirmation. If confirmed through deeper observations, this would also be a typical feature of LyC leakers (J. Chisholm et al. 2020).

All this suggests that GHZ2 could have a strong LyC output. Nevertheless, these findings also suggest that comparing with

low-redshift analogs may be a limitation, possibly due to the extremely high mass density and SFR density of GHZ2. Indeed, while some of the galaxies from S. R. Flury et al. (2022b) have O32 similar to GHZ2, none of them reach the compact star formation activity seen in this galaxy at $z = 12.34$. We also note that the $\text{C IV}_{\lambda 1549}/\text{C III}_{\lambda\lambda 1907,1909}$ ratio (another LyC leaker indicator) was measured for GHZ2 by C24, and its value of $\simeq 3$ exceeds those typically found in strong LyC leakers at $z \sim 0.3$ – 0.4 (D. Schaerer et al. 2022a).

Using this indirect derivation of f_{esc} , we can recalculate the ionizing photon production efficiency ξ_{ion} compared to the estimation in Z24, which assumes $f_{\text{esc}} = 0$. Assuming negligible dust attenuation and the M_{UV} from the companion papers, we can use the following formulation of D. Schaerer et al. (2016):

$$N_{\text{LyC}}[\text{s}^{-1}] = 2.1 \times 10^{12} (1 - f_{\text{esc}})^{-1} L(\text{H}\beta) [\text{erg s}^{-1}] \quad (1)$$

and

$$\log(\xi_{\text{ion}}) = \log(N_{\text{LyC}}) + 0.4 \times M_{\text{UV}} - 20.64, \quad (2)$$

where N_{LyC} is the number of ionizing photons produced per unit time, obtaining $\log(\xi_{\text{ion}}) = 25.72^{+0.35}_{-0.15}$, which is consistent with the lower limit of 25.3 derived in Z24. This is comparable to values typically measured in Ly α emitters (Y. Harikane et al. 2018; D. Sobral & J. Matthee 2019) and in $z > 7$ galaxies with strong [O III] and UV line emission (D. P. Stark et al. 2017; R. Endsley et al. 2021). In particular, our result is very similar to the $\log(\xi_{\text{ion}}) = 25.69$ measured in a strong C IV emitter at $z = 7.045$ by D. P. Stark et al. (2015). A significant correlation was also found between ξ_{ion} , M_{*} , and Σ_{SFR} (M. Castellano et al. 2023a), with $\log(\xi_{\text{ion}}) > 25$ found in galaxies with $\Sigma_{\text{SFR}} > 10 M_{\odot} \text{ yr}^{-1} \text{ kpc}^{-2}$. The ξ_{ion} estimated for GHZ2 is thus consistent with that expected for a system with extreme Σ_{SFR} .

The absence of any Ly α emission in GHZ2 might give additional insights on the environment of this galaxy. Despite

the relatively bright magnitude and escape fraction, the age of the source is too short, and therefore there was not enough time to create a large enough ionized bubble for the Ly α to become visible. Deeper observations at higher resolution in the future could put tighter constraints on the presence of faint, highly redshifted Ly α .

3.3. Gas-phase Metallicity from Strong-line Ratios

An estimate of the metallicity of GHZ2 was already made in C24 and Z24, using the emission-line indicators available in their spectral range. In the former, they derived Z from the Ne3O2 index, the $C\text{ III}]_{\lambda 1909}/O\text{ III}]_{\lambda 1663}$ ratio, and the EW of C III]. In the latter, instead, they estimated the ISM metal content from the R3 index. Adopting a variety of calibrations available in the literature, they suggest that the metallicity of GHZ2 is in the range between $\sim 3\%$ and $\sim 12\%$ solar.

We now complement previous measurements of Z_{gas} with additional diagnostics that exploit the full NIRSpec + MIRI coverage, including in particular the R2, R23, and O32 indices. R23 is one of the most widely adopted since, including both of the main ionization stages of oxygen (O^+ and O^{++}), it is not significantly affected by the ionization structure of the H II regions. However, it has a bi-valued metallicity solution, peaking at $12 + \log(O/H) \simeq 8.0$ and decreasing toward higher and lower metallicities (R. Maiolino et al. 2008), which makes the dependence weak at the turnaround. R2 also has a quadratic behavior as a function of metallicity, but it peaks at higher metallicity ($12 + \log(O/H) \simeq 8.7$); hence, it has more constraining power at low Z . Finally, the dependence of the O32 index on metallicity is mostly secondary, as O32 depends on both Z and the ionization parameter, but it has the advantage of showing in general a monotonic increase toward lower metallicities. The combination of these three metallicity indicators with the other optical-based ones analyzed in C24 and Z24 can more tightly constrain the oxygen abundance of the galaxy, minimizing degeneracies and secondary dependences on other elements, as suggested by M. Curti et al. (2020).

To perform the calculations, we consider multiple relations, calibrated with the direct (T_e -based) method on galaxies from $z=0$ to higher redshifts for which the [O III] auroral line at 4363 Å is available. In particular, we consider the strong-line calibrations derived by M. Curti et al. (2017, 2020) from SDSS galaxies, those derived by F. Bian et al. (2018) using a BPT-selected (high-ionization and high-excitation) sample from the SDSS, and those proposed by K. Nakajima et al. (2022) using a sample of local extremely metal-poor galaxies (EMPGs). In addition, we also adopt the calibrations obtained by R. L. Sanders et al. (2024) by adding 16 high-redshift galaxies with auroral line detection recently observed by JWST to previous [O III] $_{\lambda 4363}$ -detected samples observed from the ground. The results obtained with all these estimators are summarized in Table 1, and they range from a minimum of 4% solar to a maximum of 12% solar. In all cases, the 1σ lower and upper errors on Z are derived by considering only the uncertainty of the line ratios. We also note that at $z > 10$ we expect the metal content to be significantly lower than $0.3 \times Z_{\odot}$ (G. Ucci et al. 2023); hence, we can safely assume that we are in the low-metallicity branch of the R2 and R23 relations.

We find that, within the same calibration set, the various indices tend to give metallicities that are consistent among each other, suggesting that using only one index correctly informs

the metallicity of the galaxy. A weighted average from all the available line ratios is also provided in Table 1 for each calibration set. In some cases the metallicities could not be derived, so we did not consider them in the weighted average. For example, in F. Bian et al. (2018) the R3 and R23 indices do not cover the lower branch, while adopting M. Curti et al. (2020) and K. Nakajima et al. (2022), our O32 and Ne3O2 measured values do not have a corresponding metallicity. We note that in the calibrations by K. Nakajima et al. (2022) the O32 and Ne3O2 indices show a quadratic, bi-valued behavior at low metallicity, similar to that seen for the R23 index at high Z , with a narrow allowed range for the two line ratios; hence, they would not be very informative on the chemical content of the galaxy. For these calibrations we consider the relations valid for galaxies with high $\text{EW}(H\beta) > 200$ Å. Even though this line and the underlying continuum are not detected with MIRI, the high O32 line ratio strongly suggests that we are in the high-EW($H\beta$) case, with expected values much higher than 200 Å according to the correlation shown in Figure 22 of S. R. Flury et al. (2022a).

Most of the discrepancy within the metallicity range estimated for GHZ2 comes from applying different calibration sets, as also noted in the two companion papers from individual indices. This is likely due to the different sample selection, including different redshifts and (possibly) different intrinsic physical properties of the galaxies considered for the calibrations. On average, the relations from R. L. Sanders et al. (2024) tend to give metallicities that are slightly lower by $\sim 1\% - 2\%$ compared to the median value from all the methods, while M. Curti et al. (2020) tend to give slightly higher values. This variance (although small) of metallicity estimates highlights the challenge of finding local samples that truly reflect the characteristics of high-redshift galaxies, particularly those more extreme at $z > 10$, as also discussed in previous sections.

Taking the weighted averages together, the different calibrations suggest that the metallicity of GHZ2 comprises between 5% and 11% solar, consistent with the previous estimation in C24 and Z24. If we further average these results, we obtain a metallicity of $0.06^{+0.02}_{-0.01} Z_{\odot}$. This is slightly above but also consistent with the metallicity of $0.04^{0.07}_{0.02}$ derived by C24 from SED fitting.

The metallicity of GHZ2 is very low, although not significantly different from some EMPGs discovered at the EoR (D. Schaerer et al. 2022b; K. Z. Arellano-Córdova et al. 2022; D. Langeroodi et al. 2023; J. Brinchmann 2023; J. E. Rhoads et al. 2023; K. Nakajima et al. 2023; T. Morishita & M. Stiavelli 2023), or in very low mass galaxies at low and intermediate redshift (e.g., R. Amorín et al. 2012, 2015; A. Calabrò et al. 2017; R. Amorín et al. 2017). This result also suggests that GHZ2, despite the very young age of the Universe at $z \sim 12$, already contains chemically enriched gas.

3.4. Electron Temperature and T_e -based Metallicity

Compared to our companion papers (C24 and Z24), the combination of NIRSpec and MIRI allows us to estimate the electron temperature of the gas from the $O\text{ III}]_{\lambda 1666}/[O\text{ III}]_{\lambda 5007}$ observed line ratio of 0.09 ± 0.02 and, consequently, the gas-phase metallicity using the direct (T_e -based) method.

For the calculation of the metallicity, we use the Python package `pyneb`. We first assume that the gas has an electron density of 10^3 cm^{-3} , as suggested by the ALMA data and by the comparison with photoionization models. Then, we derive

the electron temperature of O^{2+} , $T_e([O III])$, from $O III]_{\lambda 1666}/[O III]_{\lambda 5007}$, adopting the collision strengths from K. M. Aggarwal & F. P. Keenan (1999). This yields $T_e([O III]) = 21,200_{-2400}^{+2700}$ K. Regarding the temperature of O^+ , $T_e([O II])$, given the nondetection of low-ionization auroral lines (e.g., $[O II]_{\lambda\lambda 7322,7332}$), we infer it in an indirect way from $T_e([O III])$ using the relation of A. Campbell et al. (1986):

$$T_e(O II) = 0.7 \times T_e(O III) + 3000 \text{ K}, \quad (3)$$

as done by R. L. Sanders et al. (2024) for galaxies up to redshift ~ 9 . However, we note that the results would not significantly change if we instead assume $T_e([O II]) = T_e([O III])$.

For the calculation of the oxygen abundance, we assume that O^{3+} is negligible and that all O is in the form of O^{2+} or O^+ , which is valid also in galaxies with extremely high ionization conditions, as suggested by some recent works (e.g., D. A. Berg et al. 2018, 2021). Using the electron temperatures estimated above, we finally derive the O^{2+}/H^+ and the $O^+/H\beta$ ratios from $[O III]_{\lambda 5007}/H\beta$ and $[O II]_{\lambda 3727}/H\beta$, respectively. This yields an oxygen abundance (with the direct method) of $12 + \log(O/H) = 7.44_{-0.24}^{+0.26}$, that is, $0.06_{-0.02}^{+0.04} Z_{\odot}$. This result is remarkably consistent with the metallicity derived by combining all five strong-line indicators (using the R. L. Sanders et al. 2024 calibration), as shown in Table 1, corroborating the very metal-poor nature of GHZ2.

4. Conclusions

The combination of two instruments, NIRSpec and MIRI, in addition to the unique sensitivity of JWST in the near-infrared, has allowed us for the first time to probe the full rest-frame UV and optical spectral properties for a galaxy at $z > 10$. The galaxy GHZ2/GLASSz-12, one of the brightest galaxies discovered during the first JWST imaging campaigns, was confirmed to have a spectroscopic redshift of 12.34 (from C24 and Z24). Leveraging this unique data set, we have investigated the ionization and metallicity properties of this galaxy in a comprehensive way, shedding light on the ISM conditions in pre-EoR.

Combining six rest-frame optical indices, we have found that GHZ2 has very strong ionizing conditions as probed by extreme O32 and Ne3O2 line ratios (~ 1.4 and ~ 0.4 , respectively). These values are consistent with photoionization by either an AGN or star formation, which we are not able to discriminate with the NIRSpec + MIRI spectra. Assuming photoionization from young massive stars, the line ratios suggest that the ionization parameter is very high between $\log(U) = -2$ and -1.5 , surpassing the average values found in star-forming galaxies at the EoR and in local analogs of high-redshift galaxies. One possible underlying physical reason for these rather unique ionizing properties of GHZ2 is that the star formation of the whole galaxy is still confined in a very compact radius. The very high Σ_{SFR} ($\sim 10^2 - 10^3 M_{\odot} \text{ yr}^{-1} \text{ kpc}^{-2}$) and Σ_{M_*} ($\sim 10^4 - 10^5 M_{\odot} \text{ pc}^{-2}$), the high ionizing photon production efficiency ($\log(\xi_{\text{ion}}) \simeq 25.7$), and the high gas densities ($10^3 \text{ cm}^{-3} < n_e < 10^4 \text{ cm}^{-3}$) suggested by the nebular line ratios (also including ALMA data) are additional indicators of an extreme star formation scenario that is not typical of galaxies at lower redshifts. A similarly high density of SF and M_* has been found only in very few systems at $z < 10$, such as in an extremely dense UV-bright starburst at $z = 3.6$ analyzed by R. Marques-Chaves et al. (2022), and in RXCJ2248-ID, which shows even more extreme Σ_{SFR} ($> 10^4 M_{\odot} \text{ yr}^{-1} \text{ kpc}^{-2}$) and ionizing conditions than GHZ2 (M. W. Topping et al. 2024).

These properties are in agreement with a scenario in which the galaxy has recently undergone a phase of elevated, very compact star formation activity that has very rapidly enriched the ISM metallicity at the level of $\sim 5\% - 10\%$ solar. This physical configuration also suggests that GHZ2 might be among the first promising candidates to start reionizing and polluting the surrounding intergalactic medium (IGM) before the EoR, possibly through radiatively driven winds from young massive stars in the recent past, as suggested by some recent models (A. Ferrara 2023; A. Ferrara et al. 2023). The negligible dust attenuation ($A_V \leq 0.1$ mag) estimated for GHZ2 in C24 and Z24 is consistent with a dust clearing outflow scenario outlined by those models. The escape fraction of 0.1, estimated from a variety of indirect indicators, indicates that the galaxy may have created channels for the leaking of ionizing photons, which is another prediction of the above models. The lack of Ly α suggests that GHZ2 is rather isolated and has not yet created a large ionized bubble required for that line to transmit in a completely neutral IGM expected at $z \simeq 12$. We also note that even though the specific SFR (sSFR) of $\log(\text{sSFR}/\text{yr}^{-1}) = -8.10_{-0.27}^{+0.54}$ is currently below the super-Eddington threshold proposed by A. Ferrara (2023), it might exceed that limit according to alternative M_* estimations by Z24, or it might have reached those conditions in the past, depending on the exact shape of the SFH.

The combination of the NIRSpec and MIRI spectra for GHZ2 provides a unique insight to investigate the physical properties of galaxies at $z > 10$, which has become the next challenge for JWST. First, the UV-to-optical combined diagnostics yield ionization and metallicity properties that are in agreement with those estimated with UV-only or optical-only indicators. This suggests that analysis of a limited region of the spectrum, such as that still accessible with NIRSpec at very high redshift, provides reliable results and, at the same time, an effective way to characterize statistically meaningful samples of objects in the pre-reionization cosmic phase. Nevertheless, MIRI could be used on the brightest galaxies to further test the consistency of the UV and optical diagnostics.

Second, despite the large wavelength coverage of the NIRSpec + MIRI combined observations, UV+optical indicators still fail to unambiguously assess the nature of the ionizing source, as they cannot discriminate between an AGN and star formation in a low-metallicity, high-density, and extreme-ionization environment. Deeper observations at high resolution targeting broad components of the C IV and Balmer lines and fainter high-ionization lines in the UV-to-optical range are likely required if we want to clarify the ionizing mechanism of the earliest galaxies.

Finally, the extreme emission-line properties and ionizing conditions of GHZ2 when compared to galaxies at lower redshifts suggests that the consolidated approach of using nebular line ratios of local, low-mass, metal-poor systems to infer the properties of high- z galaxies might have reached its limits when coming to extreme redshifts ($z \gtrsim 10$). This is due to the extremely dense ISM and star formation that cannot be fully tested in local counterparts. Furthermore, galaxies at $z > 10$ are likely surrounded by an IGM that is still completely neutral and pristine, highlighting the stark differences in properties and environment between the two populations. The challenge of finding samples of local analogs that are truly representative of the properties of high-redshift galaxies is evident in the slight

variance observed among various metallicity calibrations. Direct observations of $z > 10$ galaxies are thus necessary.

Acknowledgments

We thank the referee for the constructive report. This work is based on observations made with the NASA/ESA/CSA James Webb Space Telescope (JWST). The data presented in this article were obtained from the Mikulski Archive for Space Telescopes (MAST) at the Space Telescope Science Institute, which is operated by the Association of Universities for Research in Astronomy, Inc., under NASA contract NAS 5-03127 for JWST. The specific observations analyzed can be accessed via doi:10.17909/4r6b-bx96 and doi:10.17909/gret-mk52. These observations are associated, respectively, with programs JWST-GO-3073 and JWST-GO-3703. We acknowledge financial support from NASA through grant JWST-ERS-1342. Support was also provided by INAF Mini-grant “Reionization and Fundamental Cosmology with High-Redshift Galaxies.” A.C. acknowledges support from the INAF Large Grant for Extragalactic Surveys with JWST. A.C. acknowledges support from the “Strengthening the Italian Leadership in ELT and SKA – STILES” project, funded by the European Union (“Next Generation-EU” program, proposal No. IR0000034). We acknowledge support from the PRIN 2022 MUR project 2022CB3PJ3, “First Light And Galaxy aSsembly (FLAGS) funded by the European Union Next Generation EU.”

ORCID iDs

Antonello Calabrò  <https://orcid.org/0000-0003-2536-1614>
 Marco Castellano  <https://orcid.org/0000-0001-9875-8263>
 Jorge A. Zavala  <https://orcid.org/0000-0002-7051-1100>
 Laura Pentericci  <https://orcid.org/0000-0001-8940-6768>
 Pablo Arrabal Haro  <https://orcid.org/0000-0002-7959-8783>
 Tom J. L. C. Bakx  <https://orcid.org/0000-0002-5268-2221>
 Denis Burgarella  <https://orcid.org/0000-0002-4193-2539>
 Caitlin M. Casey  <https://orcid.org/0000-0002-0930-6466>
 Mark Dickinson  <https://orcid.org/0000-0001-5414-5131>
 Steven L. Finkelstein  <https://orcid.org/0000-0001-8519-1130>
 Adriano Fontana  <https://orcid.org/0000-0003-3820-2823>
 Mario Llerena  <https://orcid.org/0000-0003-1354-4296>
 Sara Mascia  <https://orcid.org/0000-0002-9572-7813>
 Emiliano Merlin  <https://orcid.org/0000-0001-6870-8900>
 Ikki Mitsuhashi  <https://orcid.org/0000-0001-7300-9450>
 Lorenzo Napolitano  <https://orcid.org/0000-0002-8951-4408>
 Diego Paris  <https://orcid.org/0000-0002-7409-8114>
 Pablo G. Pérez-González  <https://orcid.org/0000-0003-4528-5639>
 Guido Roberts-Borsani  <https://orcid.org/0000-0002-4140-1367>
 Paola Santini  <https://orcid.org/0000-0002-9334-8705>
 Tommaso Treu  <https://orcid.org/0000-0002-8460-0390>
 Eros Vanzella  <https://orcid.org/0000-0002-5057-135X>

References

Aggarwal, K. M., & Keenan, F. P. 1999, *ApJS*, 123, 311
 Amorín, R., Fontana, A., Pérez-Montero, E., et al. 2017, *NatAs*, 1, 0052
 Amorín, R., Pérez-Montero, E., Contini, T., et al. 2015, *A&A*, 578, A105
 Amorín, R., Pérez-Montero, E., Vilchez, J. M., & Papaderos, P. 2012, *ApJ*, 749, 185
 Arellano-Córdova, K. Z., Berg, D. A., Chisholm, J., et al. 2022, *ApJL*, 940, L23

Arrabal Haro, P., Dickinson, M., Finkelstein, S. L., et al. 2023a, *ApJL*, 951, L22
 Arrabal Haro, P., Dickinson, M., Finkelstein, S. L., et al. 2023b, *Natur*, 622, 707
 Asplund, M., Grevesse, N., Sauval, A. J., & Scott, P. 2009, *ARA&A*, 47, 481
 Atek, H., Chemerynska, I., Wang, B., et al. 2023, *MNRAS*, 524, 5486
 Backhaus, B. E., Trump, J. R., Cleri, N. J., et al. 2022, *ApJ*, 926, 161
 Bakx, T. J. L. C., Zavala, J. A., Mitsuhashi, I., et al. 2023, *MNRAS*, 519, 5076
 Behroozi, P., Conroy, C., Wechsler, R. H., et al. 2020, *MNRAS*, 499, 5702
 Berg, D. A., Chisholm, J., Erb, D. K., et al. 2021, *ApJ*, 922, 170
 Berg, D. A., Erb, D. K., Auger, M. W., et al. 2018, *ApJ*, 859, 164
 Bergamini, P., Acebron, A., Grillo, C., et al. 2023, *ApJ*, 952, 84
 Bian, F., Kewley, L. J., & Dopita, M. A. 2018, *ApJ*, 859, 175
 Bouwens, R. J., Stefanon, M., Brammer, G., et al. 2023, *MNRAS*, 523, 1036
 Brinchmann, J. 2023, *MNRAS*, 525, 2087
 Bruzual, G., & Charlot, S. 2003, *MNRAS*, 344, 1000
 Bunker, A. J., Saxena, A., Cameron, A. J., et al. 2023, *A&A*, 677, A88
 Bushouse, H., Eisenhamer, J., Dencheva, N., et al. 2024, JWST Calibration Pipeline v1.13.4, Zenodo, doi:10.5281/zenodo.10569856
 Calabrò, A., Amorín, R., Fontana, A., et al. 2017, *A&A*, 601, A95
 Calabrò, A., Pentericci, L., Feltre, A., et al. 2023, *A&A*, 679, A80
 Calabrò, A., Pentericci, L., Santini, P., et al. 2024, *A&A*, 690, A290
 Cameron, A. J., Saxena, A., Bunker, A. J., et al. 2023, *A&A*, 677, A115
 Campbell, A., Terlevich, R., & Melnick, J. 1986, *MNRAS*, 223, 811
 Cappelluti, N., Hasinger, G., & Natarajan, P. 2022, *ApJ*, 926, 205
 Carnall, A. C., McLure, R. J., Dunlop, J. S., & Davé, R. 2018, *MNRAS*, 480, 4379
 Casey, C. M., Akims, H. B., Shuntov, M., et al. 2024, *ApJ*, 965, 98
 Castellano, M., Belfiori, D., Pentericci, L., et al. 2023a, *A&A*, 675, A121
 Castellano, M., Fontana, A., Treu, T., et al. 2022, *ApJL*, 938, L15
 Castellano, M., Fontana, A., Treu, T., et al. 2023b, *ApJL*, 948, L14
 Castellano, M., Napolitano, L., Fontana, A., et al. 2024, *ApJ*, 972, 143
 Chabrier, G. 2003, *PASP*, 115, 763
 Chatzikos, M., Bianchi, S., Camilloni, F., et al. 2023, *RMxAA*, 59, 327
 Chisholm, J., Prochaska, J. X., Schaerer, D., Gazagnes, S., & Henry, A. 2020, *MNRAS*, 498, 2554
 Chisholm, J., Saldana-Lopez, A., Flury, S., et al. 2022, *MNRAS*, 517, 5104
 Cleri, N. J., Olivier, G. M., Hutchison, T. A., et al. 2023, *ApJ*, 953, 10
 Curti, M., Cresci, G., Mannucci, F., et al. 2017, *MNRAS*, 465, 1384
 Curti, M., D’Eugenio, F., Camiani, S., et al. 2023, *MNRAS*, 518, 425
 Curti, M., Maiolino, R., Curtis-Lake, E., et al. 2024, *A&A*, 684, A75
 Curti, M., Mannucci, F., Cresci, G., & Maiolino, R. 2020, *MNRAS*, 491, 944
 De Cia, A., Ledoux, C., Mattsson, L., et al. 2016, *A&A*, 596, A97
 Ding, X., Birrer, S., Treu, T., et al. 2021, arXiv:2111.08721
 Donnan, C. T., McLeod, D. J., Dunlop, J. S., et al. 2023a, *MNRAS*, 518, 6011
 Donnan, C. T., McLeod, D. J., McLure, R. J., et al. 2023b, *MNRAS*, 520, 4554
 Eldridge, J. J., Stanway, E. R., Xiao, L., et al. 2017, *PASA*, 34, e058
 Endsley, R., Stark, D. P., Chevillard, J., & Charlot, S. 2021, *MNRAS*, 500, 5229
 Feltre, A., Charlot, S., & Gutkin, J. 2016, *MNRAS*, 456, 3354
 Ferland, G. J., Chatzikos, M., Guzmán, F., et al. 2017, *RMxAA*, 53, 385
 Ferrara, A. 2024, *A&A*, 684, A207
 Ferrara, A., Pallottini, A., & Dayal, P. 2023, *MNRAS*, 522, 3986
 Finkelstein, S. L., Bagley, M. B., Arrabal Haro, P., et al. 2022, *ApJL*, 940, L55
 Finkelstein, S. L., Bagley, M. B., Ferguson, H. C., et al. 2023, *ApJL*, 946, L13
 Flury, S. R., Jaskot, A. E., Ferguson, H. C., et al. 2022a, *ApJ*, 930, 126
 Flury, S. R., Jaskot, A. E., Ferguson, H. C., et al. 2022b, *ApJS*, 260, 1
 Franco, M., Akims, H. B., Casey, C. M., et al. 2024, *ApJ*, 973, 23
 Groves, B. A., Dopita, M. A., & Sutherland, R. S. 2004, *ApJS*, 153, 75
 Gutkin, J., Charlot, S., & Bruzual, G. 2016, *MNRAS*, 462, 1757
 Harikane, Y., Inoue, A. K., Mawatari, K., et al. 2022, *ApJ*, 929, 1
 Harikane, Y., Nakajima, K., Ouchi, M., et al. 2024, *ApJ*, 960, 56
 Harikane, Y., Ouchi, M., Oguri, M., et al. 2023, *ApJS*, 265, 5
 Harikane, Y., Ouchi, M., Shibuya, T., et al. 2018, *ApJ*, 859, 84
 Heckman, T. M. 2001, in ASP Conf. Ser. 240, Gas and Galaxy Evolution, ed. J. E. Hibbard, M. Rupen, & J. H. van Gorkom (San Francisco, CA: ASP), 345
 Hsiao, T. Y.-Y., Abdurro’uf, Coe, D., et al. 2024, *ApJ*, 973, 8
 Izotov, Y. I., Schaerer, D., Worseck, G., et al. 2020, *MNRAS*, 491, 468
 Jaskot, A. E., & Oey, M. S. 2013, *ApJ*, 766, 91
 Jiang, T., Malhotra, S., Yang, H., & Rhoads, J. E. 2019, *ApJ*, 872, 146
 Kauffmann, G., Heckman, T. M., White, S. D. M., et al. 2003, *MNRAS*, 341, 33
 Kewley, L. J., & Ellison, S. L. 2008, *ApJ*, 681, 1183
 Kocevski, D. D., Onoue, M., Inayoshi, K., et al. 2023, *ApJL*, 954, L4
 Langeroodi, D., Hjorth, J., Chen, W., et al. 2023, *ApJ*, 957, 39

- Larson, R. L., Finkelstein, S. L., Kocevski, D. D., et al. 2023, *ApJL*, **953**, L29
- Liu, X.-W., & Danziger, J. 1993, *MNRAS*, **261**, 465
- Ma, X., Hopkins, P. F., Faucher-Giguère, C.-A., et al. 2016, *MNRAS*, **456**, 2140
- Maiolino, R., Nagao, T., Grazian, A., et al. 2008, *A&A*, **488**, 463
- Marques-Chaves, R., Schaerer, D., Alvarez-Marquez, J., et al. 2022, *MNRAS*, **517**, 2972
- Mascia, S., Pentericci, L., Calabrò, A., et al. 2023, *A&A*, **672**, A155
- Mason, C. A., Trenti, M., & Treu, T. 2023, *MNRAS*, **521**, 497
- McClymont, W., Tacchella, S., D'Eugenio, F., et al. 2024, arXiv:2405.15859
- Merlin, E., Santini, P., Paris, D., et al. 2024, arXiv:2409.0016
- Morishita, T., & Stiavelli, M. 2023, *ApJL*, **946**, L35
- Naidu, R. P., Oesch, P. A., van Dokkum, P., et al. 2022, *ApJL*, **940**, L14
- Naidu, R. P., Tacchella, S., Mason, C. A., et al. 2020, *ApJ*, **892**, 109
- Nakajima, K., Ellis, R. S., Robertson, B. E., Tang, M., & Stark, D. P. 2020, *ApJ*, **889**, 161
- Nakajima, K., Ouchi, M., Isobe, Y., et al. 2023, *ApJS*, **269**, 33
- Nakajima, K., Ouchi, M., Xu, Y., et al. 2022, *ApJS*, **262**, 3
- Napolitano, L., Pentericci, L., Santini, P., et al. 2024, *A&A*, **688**, A106
- Oke, J. B., & Gunn, J. E. 1983, *ApJ*, **266**, 713
- Ono, Y., Harikane, Y., Ouchi, M., et al. 2023, *ApJ*, **951**, 72
- Onodera, M., Carollo, C. M., Lilly, S., et al. 2016, *ApJ*, **822**, 42
- Osterbrock, D. E., & Ferland, G. J. 2006, *Astrophysics of Gaseous Nebulae and Active Galactic Nuclei* (Mill Valley, CA: Univ. Science Books)
- Pahl, A. J., Shapley, A., Faisst, A. L., et al. 2020, *MNRAS*, **493**, 3194
- Papovich, C., Simons, R. C., Estrada-Carpenter, V., et al. 2022, *ApJ*, **937**, 22
- Pellegrini, E. W., Oey, M. S., Winkler, P. F., et al. 2012, *ApJ*, **755**, 40
- Pereira, C. B., de Araújo, F. X., & Landaberry, S. J. C. 1999, *MNRAS*, **309**, 1074
- Pérez-González, P. G., Gil de Paz, A., Zamorano, J., et al. 2003, *MNRAS*, **338**, 508
- Plat, A., Charlot, S., Bruzual, G., et al. 2019, *MNRAS*, **490**, 978
- Pontoppidan, K. M., Barrientes, J., Blome, C., et al. 2022, *ApJL*, **936**, L14
- Popping, G. 2023, *A&A*, **669**, L8
- Reddy, N. A., Topping, M. W., Sanders, R. L., Shapley, A. E., & Brammer, G. 2023, *ApJ*, **952**, 167
- Reddy, N. A., Topping, M. W., Shapley, A. E., et al. 2022, *ApJ*, **926**, 31
- Rhoads, J. E., Wold, I. G. B., Harish, S., et al. 2023, *ApJL*, **942**, L14
- Roberts-Borsani, G., Treu, T., Shapley, A., et al. 2024, arXiv:2403.07103
- Sanders, R. L., Shapley, A. E., Kriek, M., et al. 2016, *ApJ*, **816**, 23
- Sanders, R. L., Shapley, A. E., Topping, M. W., Reddy, N. A., & Brammer, G. B. 2024, *ApJ*, **962**, 24
- Scarlata, C., Hayes, M., Panagia, N., et al. 2024, arXiv:2404.09015
- Schaerer, D., Izotov, Y. I., Verhamme, A., et al. 2016, *A&A*, **591**, L8
- Schaerer, D., Izotov, Y. I., Worseck, G., et al. 2022a, *A&A*, **658**, L11
- Schaerer, D., Marques-Chaves, R., Barrufet, L., et al. 2022b, *A&A*, **665**, L4
- Selvelli, P., Danziger, J., & Bonifacio, P. 2007, *A&A*, **464**, 715
- Sharma, M., Theuns, T., Frenk, C., et al. 2017, *MNRAS*, **468**, 2176
- Shimakawa, R., Kodama, T., Steidel, C. C., et al. 2015, *MNRAS*, **451**, 1284
- Sobral, D., & Matthee, J. 2019, *A&A*, **623**, A157
- Stanway, E. R., & Eldridge, J. J. 2018, *MNRAS*, **479**, 75
- Stark, D. P., Ellis, R. S., Charlot, S., et al. 2017, *MNRAS*, **464**, 469
- Stark, D. P., Walth, G., Charlot, S., et al. 2015, *MNRAS*, **454**, 1393
- Stiavelli, M., Morishita, T., Chiaberge, M., et al. 2023, *ApJL*, **957**, L18
- Topping, M. W., Stark, D. P., Senchyna, P., et al. 2024, *MNRAS*, **529**, 3301
- Treu, T., Roberts-Borsani, G., Bradac, M., et al. 2022, *ApJ*, **935**, 110
- Trinca, A., Schneider, R., Maiolino, R., et al. 2023, *MNRAS*, **519**, 4753
- Trump, J. R., Arrabal Haro, P., Simons, R. C., et al. 2023, *ApJ*, **945**, 35
- Ucci, G., Dayal, P., Hutter, A., et al. 2023, *MNRAS*, **518**, 3557
- Vladilo, G., Abate, C., Yin, J., et al. 2011, *A&A*, **530**, A33
- Yanagisawa, H., Ouchi, M., Nakajima, K., et al. 2024, *ApJ*, **974**, 180
- Yang, L., Morishita, T., Leethochawalit, N., et al. 2022, *ApJL*, **938**, L17
- Zavala, J. A., Castellano, M., Akins, H. B., et al. 2024, arXiv:2403.10491
- Zeimann, G. R., Ciardullo, R., Gebhardt, H., et al. 2015, *ApJ*, **798**, 29